

# Periodic Research

## Crystallographic and Magnetic Studies of Cr<sup>3+</sup> Substituted Nanocrystalline Cobalt Manganese Ferrites

### Abstract

Nanocrystalline ferrites having composition  $\text{CoMn}_{1-x}\text{Cr}_x\text{FeO}_4$  ferrite, with varying concentration of chromium ( $x=0.00, 0.25, 0.50, 0.75$  and  $1.00$ ) were synthesized by sol-gel method, resulting single phase cubic spinels. The unit cell parameter decreases with increases in  $\text{Cr}^{3+}$  substitution. T.E.M studies reveals the Nanocrystalline nature of synthesized samples. The I.R absorption spectra of all investigated ferrite samples shows two strong absorption bands at  $716-748\text{ cm}^{-1}$  due to intrinsic vibrations of the tetrahedral group and second band in the range of  $294-375\text{ cm}^{-1}$  is due to octahedral metal complexes. The magnetic properties were measured by vibrating sample magnetometer, indicating, the saturation magnetization decreases with increases in concentration of  $\text{Cr}^{3+}$  ion, due to weaker magnetic moment of  $\text{Cr}^{3+}$  ion as compare to  $\text{Mn}^{3+}$  ions.

**Keywords:** Nanocrystalline magnetic material, sol-gel synthesis, X-ray analysis, T.E.M analysis, I.R spectroscopy, magnetic properties.

### M. M. Langade

Deptt. of Chemistry,  
Jawahar Art, Science and  
Commerce College  
Anadur, (M.S.)

### Introduction

Cobalt ferrite ( $\text{CoFe}_2\text{O}_4$ ) corresponds to the group of spinel-type ferrites, which are compounds with a cubic oxygen lattice of the general formula  $\text{Me}_x\text{Fe}_{3-x}\text{O}_4$  [1], where Me is usually a divalent metal cation. The properties of ferrites are mainly depending upon chemical composition, method of preparation, sintering time and temperature [2]. Introducing small amount of a foreign ion can change the electrical and magnetic properties of the ferrite [3].  $\text{CoMn}_{1-x}\text{Cr}_x\text{FeO}_4$  spinel ferrite nano particulate system may offers an opportunity to study the roles of  $\text{Co}^{2+}$ ,  $\text{Mn}^{3+}$  and  $\text{Fe}^{3+}$  in spinel ferrites through the variation of  $\text{Cr}^{3+}$  ion concentration.

### Experimental

The wide applications of nano crystalline ferrites lead to the development of various synthesis methods, which include hydrothermal, ultrasonically assisted hydrothermal, mechanical alloying, pulsed wire discharge, shockwave, reverse micelle co-precipitation, freeze drying, spray drying, precursor and sol-gel [4-6]. The sol-gel method, in particular, is one of the most useful and attractive techniques for the synthesis of nano crystalline ferrite materials because of its advantages such as; good stoichiometric control and the production of nanocrystalline particles.

Analytical grade reagents, cobalt nitrate ( $\text{Co}(\text{NO}_3)_2 \cdot 3\text{H}_2\text{O}$ ), chromium nitrate ( $\text{Cr}(\text{NO}_3)_3 \cdot 9\text{H}_2\text{O}$ ), manganese nitrate ( $\text{Mn}(\text{NO}_3)_2 \cdot 6\text{H}_2\text{O}$ ), iron nitrate ( $\text{Fe}(\text{NO}_3)_3 \cdot 9\text{H}_2\text{O}$ ) and citric acid ( $\text{C}_6\text{H}_8\text{O}_7 \cdot \text{H}_2\text{O}$ ), were used to synthesize the  $\text{CoMn}_{1-x}\text{Cr}_x\text{FeO}_4$  ( $x = 0.0, 0.25, 0.5, 0.75, 1.0$ ) ferrite nanoparticles. In the present study, sol-gel auto-combustion method was adopted to synthesize the ferrite nanoparticles. Reaction procedure was carried out in air atmosphere without protection of inert gases. The molar ratio of metal nitrates to citric acid was taken as 1:3. The metal nitrates were dissolved together in a minimum amount of double distilled water to get a clear solution. An aqueous solution of citric acid was mixed with metal nitrates solution, then ammonia solution was slowly added to adjust the pH at 7. Then the solution was heated at  $90\text{ }^\circ\text{C}$  to transform into gel. When ignited at any point of the gel, the dried gel burnt in a self-propagating combustion manner until all gel was completely burnt out to form a fluffy loose powder. The auto-combustion was completed within a minute, yielding the brown-colored ash termed as a precursor. It has been observed that the calcinations temperature is an important parameter during the synthesis of ferrite nanoparticles via sol-gel method which affects the physical and magnetic properties of ferrite nanoparticles. Therefore, the as prepared ferrite powder was annealed at  $600\text{ }^\circ\text{C}$  for 4 h in order to complete the crystallization.

### D. V. Mane

Deptt. of Chemistry,  
S.C.S. College Omega  
(M.S.)

The crystal structure of the as-prepared samples was characterized by X-ray diffraction technique using Phillips X-ray diffractometer (Model 3710) equipped with Cu-K $\alpha$  radiation ( $\lambda=1.5405\text{\AA}$ ). The microstructure was examined on the fracture surfaces of the samples using thermal field emission scanning electron microscope (SEM). Transmission electron microscope (TEM) measurements were recorded on Philips (Model CM 200).. The infrared spectra of all the samples were recorded at room temperature in the range 300  $\text{cm}^{-1}$  to 800  $\text{cm}^{-1}$  using Perkin Elmer infrared spectrophotometer. Room temperature magnetization of the samples was measured using the pulse field magnetization set-up.

## Results and Discussion Structural Analysis

Fig.1. shows X-ray diffraction pattern for all the investigated samples. The indexing the XRD pattern indicates the nominal composition structure is single-phase cubic spinel structure with Fd $3m$  cubic spinel space group. The reflection from the planes, (2 2 0), (3 1 1), (2 2 2), (4 0 0), (4 2 2), (3 3 3) and (4 4 0) appeared for all samples.

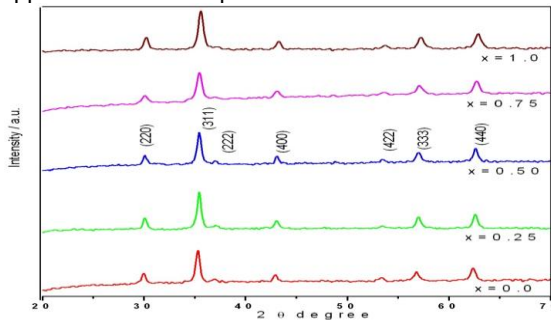


**Fig. 1.** X-Ray diffraction patterns of for  $\text{CoMn}_{1-x}\text{Cr}_x\text{FeO}_4$  ( $x=0.00, 0.25, 0.50, 0.75$  and  $1.00$ )

The values of lattice parameter ( $a$ ) were obtained by fitting the diffracted peaks using standard least-squares method and by employing eq. 1 are listed in Table .1.

$$a = \frac{\lambda \sqrt{(h^2 + k^2 + l^2)}}{2 \sin \theta} \quad 1$$

Where  $d$  is the inter-planer spacing and  $(hkl)$  is the index of XRD reflection peak.

The variation of lattice constant with increasing  $\text{Cr}^{3+}$  substitution can be explained on the basis of ionic radii of the impurity ions. The Pauling ionic radius of  $\text{Cr}^{3+}$  ( $0.63\text{\AA}$ ) is smaller than that of  $\text{Mn}^{3+}$  ( $0.66\text{\AA}$ ) ions. If the radius of the impurity ion is smaller than the displaced ion, the lattice shrinks and the lattice constant decreases.

The X-ray density ( $d_x$ ) of all the samples of the series was obtained by the following relation, are presented in Table .1.

$$d_x = \frac{8M}{Na^3} \quad 2$$

where '8' is the number of molecules per unit cell, 'M' is the molecular weight of sample, 'N' is the Avogadro's number and 'a' is lattice constant.

X-ray density increases with increase  $\text{Cr}^{3+}$  concentration, while the lattice parameter ( $a$ ) shows

opposite behavior. This causes a decrease in the size of the unit cell and consequently, it causes an increase of the X-ray density. Secondly the variation may be related to the difference in the atomic weights between  $\text{Cr}^{3+}$  and  $\text{Mn}^{3+}$  ions.

The crystallite size of the nanocrystalline samples were measured from XRD line broadening analysis applying Scherrer's formula [3]:

$$D_{XRD} = \frac{k\lambda}{\beta \cos \theta} \quad 3$$

Where  $D_{XRD}$  is the dimension of the crystallite,  $\lambda$  is wavelength of the X-ray radiation,  $\theta$  is the Bragg angle,  $k$  is a shape factor taken to be 0.94 and  $\beta$  is peak width measured at half of the maximum intensity.

Crystallite size ( $D_{XRD}$ ) from the XRD data is the utilization of the Scherrer formula (eq.3) [45]. The peaks of (2 2 0), (3 1 1), (2 2 2), (4 0 0), (4 2 2), (3 3 3) and (4 4 0) have been deconvoluted to Lorentzian curves for the determination of the crystallite size using full-width at half maximum value. It is observed from Table 1. that the  $D_{XRD}$  decreased from 19.8 ( $x = 0.0$ ) to 14.1 nm for  $x = 0.5$  and it again increased to 16.3 nm for  $x = 1.0$ . It can be concluded that the replacement of  $\text{Mn}^{3+}$  ions with  $\text{Cr}^{3+}$  in Co-Mn ferrite may leads to a decrease in cation vacancies and in turn to a decrease of crystallite size.

The percentage porosity (P) is calculated using the following relation, and tabulated in Table 1.

$$P = \left( \frac{d_x - d_B}{d_x} \right) \times 100 \quad 4$$

Where  $d_x$  and  $d_B$  are the X-ray density and bulk density respectively.

| Comp. x | a (Å)  | $d_x$ ( $\text{g/cm}^3$ ) | $D_{XRD}$ (nm) | $d_B$ ( $\text{g/cm}^3$ ) | P (%) |
|---------|--------|---------------------------|----------------|---------------------------|-------|
| 0.00    | 8.3972 | 5.243                     | 19.8           | 4.121                     | 21.41 |
| 0.25    | 8.3882 | 5.244                     | 18.5           | 4.112                     | 21.58 |
| 0.50    | 8.3717 | 5.258                     | 14.1           | 4.109                     | 21.86 |
| 0.75    | 8.3588 | 5.266                     | 16.6           | 4.107                     | 22.01 |
| 1.00    | 8.3566 | 5.253                     | 16.3           | 4.107                     | 21.82 |

**Table.1.** Lattice constant ( $a$ ), X-ray density ( $d_x$ ), crystallite size ( $D_{XRD}$ ), bulk density ( $d_B$ ) and porosity (P) of  $\text{CoMn}_{1-x}\text{Cr}_x\text{FeO}_4$

The  $\text{Cr}^{3+}$  substitution enhance the porosity thus decreasing the density of the sample. Since the decrease of bulk density is in order  $0.014 \text{ g/cm}^3$  with Cr substitution while the increase of X-ray density for  $x=0.0$  to  $x=0.75$  is of order  $0.022 \text{ g/cm}^3$ , one can expect the porosity to increase with increasing Cr substitution

In order to investigate the particle morphology and confirm the phase structure of the sol-gel synthesized Co-Mn ferrite nano particle samples, selected samples were examined by high magnification TEM. Results are also helpful in order to clarify the nanostructure of ferrite magnetic nanoparticles prepared by sol-gel method. It is observed from Fig.2, the magnetic nanoparticles are aggregated.

# Periodic Research

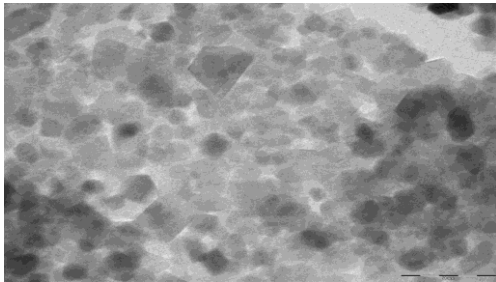


**Fig. 2.** Transmission electron micrograph (TEM) image of  $x = 1.0$  for  $\text{CoMn}_{1-x}\text{Cr}_x\text{FeO}_4$

The average values of the nanocrystalline particles are consistent with the result obtained from XRD analysis. It is evident that the magnetic nanoparticles are not exactly spherical in shape. With the observation of ferrite nanoparticles, the shape of the spinel crystal is FCC structure. It can also be seen from TEM images that the ferrite nano particles are uniform in both morphology and particle size, but agglomerated to some extent due to the interaction between magnetic nanoparticles.

It has been reported that the hopping length ' $L_A$  and  $L_B$ ' (i.e. the distance between the magnetic ions) of electrons influences the physical properties of the ferrite system. Electrons those are hopping between B- and A-sites are less probable compared to that between B- and B-sites, because the distance between the two metal ions placed in B-sites is smaller than they were placed, one in B-sites and the other in A-sites. ' $L$ ' of the A- and B-sites is determined from the relations 5 and .6.

$L_A$  and  $L_B$  i.e. the hopping length for tetrahedral A- and octahedral B-sites respectively were calculated using the following relation:[5,6]

$$L_A = a\sqrt{\frac{3}{4}} \quad 5 \qquad L_B = a\sqrt{\frac{2}{4}} \quad 6$$

Using the experimental values of lattice constant ' $a$ ', oxygen positional parameter ' $u$ ' (0.375 Å) and substituting using the following equations, the allied parameters such as tetrahedral and octahedral bond length ( $d_{AX}$  and  $d_{BX}$ ), tetrahedral edge, shared and unshared octahedral edge ( $d_{AXE}$ ,  $d_{BXE}$ ,  $d_{BXES}$  and  $d_{BXEU}$ ) were calculated [7,8,9,10&11]

$$d_{AX} = a\sqrt{3}\left(u - \frac{1}{4}\right) \quad 7$$

$$d_{BX} = a\left[3u^2 - \left(\frac{11}{4}\right)u + \frac{43}{64}\right]^{\frac{1}{2}} \quad 8$$

$$d_{AXE} = a\sqrt{2}\left(2u - \frac{1}{2}\right) \quad 9$$

$$d_{BXE\text{shared}} = a\sqrt{2}(1 - 2u) \quad 10$$

$$d_{BXE\text{unshared}} = a\left(4u^2 - 3u + \frac{11}{16}\right)^{\frac{1}{2}} \quad 11$$

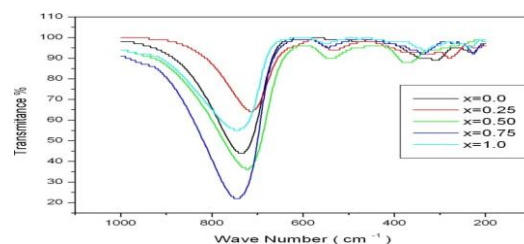
All the allied parameters; tetrahedral and octahedral bond length ( $d_{AX}$  and  $d_{BX}$ ), tetrahedral edge, shared and unshared octahedral edge ( $d_{AXE}$  and  $d_{BXE}$ ) were calculated using equations 10&11. The values of all the allied parameters are tabulated in Table 2. It is observed that  $d_{AX}$ ,  $d_{BX}$ ,  $d_{AXE}$  and  $d_{BXE}$  decrease with increasing  $\text{Cr}^{3+}$  substitution. This is due to the substitution process, that is, replacement of larger ionic radii ( $\text{Mn}^{3+}$ ) by smaller ionic radii ( $\text{Cr}^{3+}$ ) and their distribution over the tetrahedral A- and octahedral B-sites.

| Comp. x | Hopping length |           | $d_{AX}$ (Å) | $d_{BX}$ (Å) | Tetra edge (Å) | Octa edge $d_{BXE}$ (Å) |          |
|---------|----------------|-----------|--------------|--------------|----------------|-------------------------|----------|
|         | $L_A$ (Å)      | $L_B$ (Å) |              |              |                | Shared                  | unshared |
| 0.00    | 3.6361         | 2.9689    | 1.905        | 2.052        | 3.111          | 2.826                   | 2.976    |
| 0.25    | 3.6322         | 2.9657    | 1.903        | 2.050        | 3.108          | 2.823                   | 2.973    |
| 0.50    | 3.6251         | 2.9598    | 1.899        | 2.046        | 3.101          | 2.817                   | 2.967    |
| 0.75    | 3.6195         | 2.9553    | 1.897        | 2.043        | 3.097          | 2.813                   | 2.963    |
| 1.00    | 3.6185         | 2.9545    | 1.896        | 2.042        | 3.096          | 2.812                   | 2.962    |

**Table.2** Hopping lengths ( $L_A$  and  $L_B$ ), Tetrahedral bond ( $d_{AX}$ ), octahedral bond ( $d_{BX}$ ), tetra edge ( $d_{AXE}$ ) and octahedral edge ( $d_{BXE}$ ) (shared and unshared) of  $\text{CoMn}_{1-x}\text{Cr}_x\text{FeO}_4$

Infrared spectroscopy is used to detect completion of solid state reaction. The ferrite crystallizes in the natural spinel ( $\text{MgAl}_2\text{O}_4$ ) form with the space group  $\text{Fd}3m - (\text{O}_h^7)$ . On the basis of group theoretical calculations, spinel ferrites exhibit four IR active fundamentals ( $\nu$ ) in the vibrational spectra of normal as well as inverse spinel ferrites [10]. It has been reported that the first three IR bands are due to tetrahedral (A) and octahedral [B] coordination compounds, while the fourth one is due to some type of lattice vibrations involving tetrahedral cations. Fig.3

shows the IR absorption spectra of all the investigated ferrite samples, from which it can be seen that there are four bands characterizing ferrites which can easily be observed in the range  $300-800 \text{ cm}^{-1}$  for the studied samples. The positions of IR bands are listed in Table.3.



# Periodic Research

**Fig.3.**Infrared spectra of  $\text{CoMn}_{1-x}\text{Cr}_x\text{FeO}_4$ ( $x=0.00, 0.25, 0.50, 0.75$  and  $1.00$ )

| Comp. x | $\nu_1$ ( $\text{cm}^{-1}$ ) | $\nu_2$ ( $\text{cm}^{-1}$ ) | $\nu_3$ ( $\text{cm}^{-1}$ ) | $\nu_4$ ( $\text{cm}^{-1}$ ) | Ms (emu/g) | Mr (emu/g) | R     | $\eta_B$ ( $\mu_B$ ) |      | Hc (Oe) |
|---------|------------------------------|------------------------------|------------------------------|------------------------------|------------|------------|-------|----------------------|------|---------|
|         |                              |                              |                              |                              |            |            |       | Obs.                 | Cal. |         |
| 0.00    | 736                          | 314                          | 494                          | 234                          | 37.74      | 10.48      | 0.278 | 1.58                 | 3.40 | 457     |
| 0.25    | 716                          | 294                          | 533                          | 220                          | 33.22      | 9.60       | 0.289 | 1.39                 | 3.25 | 562     |
| 0.50    | 722                          | 375                          | 540                          | 307                          | 22.47      | 5.52       | 0.246 | 0.93                 | 2.80 | 239     |
| 0.75    | 745                          | 340                          | 547                          | 225                          | 13.91      | 4.64       | 0.334 | 0.58                 | 2.65 | 521     |
| 1.00    | 748                          | 337                          | 551                          | 236                          | 9.73       | 3.62       | 0.372 | 0.40                 | 2.60 | 726     |

**Table.3**

IR absorption bands, ( $\nu \text{ cm}^{-1}$ ) Saturation magnetization (Ms), remanence magnetization (Mr), remanence ratio (R), magneton number ( $\eta_B$ ) and coercivity (Hc) of  $\text{CoMn}_{1-x}\text{Cr}_x\text{FeO}_4$

The high-frequency bands,  $\nu_1$ ; is appeared in the wave number range of  $716\text{--}748 \text{ cm}^{-1}$  and is related to intrinsic vibrations of the tetrahedral group, the second band  $\nu_2$  is in the range of  $294\text{--}375 \text{ cm}^{-1}$  and is due to the octahedral metal complexes. The shoulder to the band  $\nu_1$  is appeared, this should be corresponds to low-frequency  $\nu_3$  band which is in the range of  $494\text{--}551 \text{ cm}^{-1}$ . And this  $\nu_3$  band is probably related to the divalent octahedral metal–oxygen ion complexes, the band  $\nu_4$  at  $220\text{--}307 \text{ cm}^{-1}$  was observed and can be assigned to the divalent tetrahedral vibrations. The shift in the  $\nu_1$  and  $\nu_2$  bands was found to depend on the compositions of ferrites.

The variation in the intensity of absorption band may also be related to the change of dipole moment with the internuclear distance ( $d\mu/dr$ ) [11,12]. This value represents the contribution of the ionic bond Fe–O in the lattice. So, the observed variation in the absorption band intensity with increasing  $\text{Cr}^{3+}$  substitution is presumably due to the perturbation occurring in Fe–O bonds by substitution the  $\text{Cr}^{3+}$  ions. On the other hand, the electronic distribution of Fe–O bonds is greatly affected when a  $\text{Cr}^{3+}$  ion with ( $3d^4 4s^2$ ) orbitals is introduced in its neighborhoods and this consequently affects ( $d\mu/dr$ ) of the Fe–O bond [13]. The absorption band  $\nu_1$  shifts slightly towards the higher frequency side, which can be attributed to the shifting of Fe ions towards oxygen ion on occupation of tetrahedral site by  $\text{Cr}^{3+}$  ions with smaller ionic radii, which decreases the Fe –O distance.

The magnetization curves of the  $\text{CoMn}_{1-x}\text{Cr}_x\text{FeO}_4$  spinel ferrite nanoparticle samples obtained from VSM measurements at room temperature are shown in Fig.4.

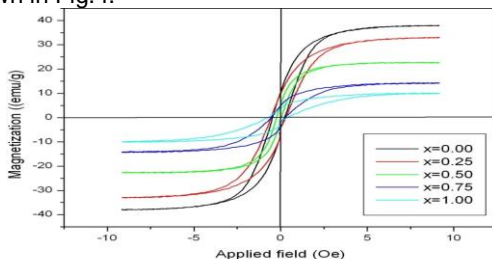


**Fig.4.**Variation of magnetization (M) with applied field (H) for  $\text{CoMn}_{1-x}\text{Cr}_x\text{FeO}_4$ ( $x=0.00, 0.25, 0.50, 0.75$  and  $1.00$ )

Substitution of  $\text{Cr}^{3+}$  ions into Co-Mn ferrite greatly affects its magnetic properties. The values of saturation magnetization (Ms), coercivity (Hc), remanence magnetization (Mr), remanence ratio (R) and magneton number ( $\eta_B$ ) obtained from magnetization plots are given in Table 3.

It is observed from the substitution of  $\text{Cr}^{3+}$  ions decreases the saturation magnetization of Co-Mn ferrite. Incorporation of more  $\text{Cr}^{3+}$  ions into the B sites weakens the L-S couplings further, probably due to the weaker magnetic moment of  $\text{Cr}^{3+}$  compared to  $\text{Mn}^{3+}$ . Such results suggest that the L-S couplings in  $\text{Cr}^{3+}$  do not benefit from its relatively large orbital angular momentum. On the other hand,  $\text{Co}^{2+}$  with a  $t_{2g}^5 e_g^2$  electron configuration in spinel has very strong L-S coupling even though it has the same number of unpaired electrons and the same theoretical orbital angular momentum as that of  $\text{Cr}^{3+}$  cation. The great difference in magnetic behavior between  $\text{Co}^{2+}$  and  $\text{Cr}^{3+}$  cations in spinel ferrite nanoparticles may offer some insights into the magnetic quantum interactions at the atomic level.

In spinel ferrite the saturation magnetization is dominated by the super exchange interactions between the tetrahedral A- and octahedral B-sites cations. Incorporation of  $\text{Cr}^{3+}$  ions will decrease the number of magnetic linkages occurring between tetrahedral and octahedral cations and thereby leads to weakening of the tetrahedral–octahedral super exchange interactions. According to Neel’s molecular-field model [14], the A-B super exchange interaction predominate the intra sublattice A-A and B-B interactions. Therefore, the net magnetic moment is given by the sum of the magnetic moments of the A and B sub lattices;  $n_{Bcal.} = M_B - M_A$ , where  $M_B$  and  $M_A$  are the B and A sub-lattice magnetic moments in  $\mu_B$ ,  $n_{Bcal.}$  Values of  $n_{Bcal.}$  were calculated using cation distribution data and by using the magnetic moment of  $\text{Fe}^{3+}$  ( $5\mu_B$ ),  $\text{Co}^{2+}$  ( $2\mu_B$ ),  $\text{Mn}^{3+}$  ( $4\mu_B$ ) and  $\text{Cr}^{3+}$  ( $3\mu_B$ ) ions.

The observed magnetic moment ( $n_{B obs.}$ ) per formula unit in the Bohr magneton ( $\mu_B$ ) was calculated using the relation [15],

$$n_{B Obs.} = \frac{(Mw) \times (Ms)}{5585} \quad 12$$

Where  $M_w$  is molecular weight of the sample  $M_s$  is the saturation magnetization.

The variation of both the magneton number values are presented in Table 3. In the present ferrite system the  $Fe^{3+}$  ions are replaced by  $Cr^{3+}$  ions, leading to a decrease in the B -site sub lattice magnetization. Therefore, the magnetization of the B sub lattices decreases, which leads to a decrease in the net magnetization. The decrease in net magnetic moment can be explained by the A-B interaction. In the presently investigated system,  $Cr^{3+}(3\mu_B)$  ions replaces  $Mn^{3+}(4\mu_B)$  ions. This replacement leads to a decrease of the magnetic moment of the B -site, and thus the magneton number  $n_B$  decreases with  $Cr^{3+}$  substitution. The decrease in  $n_{B, obs.}$  is associated mainly due to the decrease in saturation magnetization and molecular weight with  $Cr^{3+}$  substitution.

Remanence magnetization ( $M_r$ ) and remanence ratio ( $R$ ) is also decreased with the increase in  $Cr^{3+}$  substitution. Coercive field reflect the coercivity of a ferromagnetic or ferrimagnetic material. This value refers to the intensity of the magnetic field required to reduce the magnetization of the magnetic sample to zero after the magnetization of the sample has reached saturation. The coercivity increases with increasing  $Cr^{3+}$  substitution. According to the one-ion model, the anisotropy field of ferrites depends on the amount of Fe ions in the sample. It observed that the distribution of  $Co^{2+}$  and  $Fe^{3+}$  ions varies as a result of increasing  $Cr^{3+}$  substitution. This might positively contribute for anisotropy constant to increase with increasing  $Cr^{3+}$  substitution and that, consequently, the magnitude of  $H_c$  also increases. According to Stoner-Wohlfarth theory coercivity is related to anisotropy constant  $K$  through the following relation [13]:

$$H_c = \frac{0.98 \times K}{M_s} \quad 13$$

where  $K$  is the anisotropy constant and  $M_s$  is the saturation magnetization. For all concentrations of  $Cr^{3+}$  ions, the system may be considered isolated. According to this relation  $M_s$  is inversely proportional to  $H_c$ , and this is in good agreement with the present magnetic results. The coercivity also depends upon defects, surface effect, strains, non-magnetic atoms, etc. in the material [16]. The coercive force variation of the system shows a typical size dependent behavior. This behavior can be attributed to the combination of surface effect and its surface anisotropy [17]

### Conclusions

The nanoparticles of  $Cr^{3+}$  substituted Co-Mn ferrite with particle size 14-19 nm have been successfully synthesized by sol-gel auto-combustion method. The XRD pattern revealed that the cubic spinel structure is maintained for all the compositions. The particle sizes measured from XRD and TEM are in good agreement with each other. The structural parameters such as X-ray density, bulk density, and porosity were strongly affected by the incorporation of  $Cr^{3+}$  ions in Co-Mn ferrite. Hopping length i.e. jump length of ion decreased with  $Cr^{3+}$  substitution and can

be related to the smaller ionic radii associated with  $Cr^{3+}$  ions as compared to that  $Mn^{3+}$  ions. Two major absorption bands were observed in the infrared spectra and reveal the formation of single phase cubic spinel structure of  $Cr^{3+}$  substituted Co-Mn ferrite. The saturation magnetization, remanence magnetization and remanence ratio decreases linearly with increasing  $Cr^{3+}$  content. Incorporation of more  $Cr^{3+}$  ions into the B sites weakens the L-S couplings further, probably due to the weaker magnetic moment of  $Cr^{3+}$  compared to  $Mn^{3+}$ . Such results suggest that the L-S couplings in  $Cr^{3+}$  do not benefit from its relatively large orbital angular momentum. Coercivity found to enhance with  $Cr^{3+}$  substitution.

### References

1. V. N. Antonov, B. N. Harmon, V. P. Antropov, A. Y. Perlov, A. N. Yresko, Phys. Rev. B 64 (2001) 134410.
2. Sagar E Shirsath, "Synthesis condition reflected structural and magnetic properties of  $Li_{0.5}Cr_{0.5}Fe_2O_4$  nanoparticles" in 'Magnetic Nanoparticles: Properties, Synthesis and Applications' edited by Beate Acklin and Edon Lautens, Nova publishers, New York, 2012.
3. Sagar E. Shirsath, Yukiko Yasukawa, Ali Ghasemi, Xiaoxi Liu, and Akimitsu Morisako, J. Appl. Phys. 115 (2014) 17A515
4. Y. Kinemuchi, K. Ishizaka, H. Suematsu, W. Jiang, K. Yatsui, Thin Solid Films 407(2002) 109.
5. J. Zhou, J. Ma, C. Sun, L. Xie, Z. Zhao, H. Tian, J. Am. Ceram. Soc. 88 (2005) 3535.
6. P.E. Meskin, V.K. Ivanov, A.E. Barantchikov, B.R. Churagulov, Y.D. Tretyakov, Ultrason. Sonochem. 13 (2006) 4.
7. B. D. Cullity, Elements of X-ray diffraction, Addison-Wesley, London, 1959.
8. R. Valenzuela, Magnetic ceramics, Cambridge University Press, 1994.
9. R.H. Kadam, Kirti Desai, Suprya R. Kadam, Sagar E. Shirsath, Solid State Science, 269(2013) 31-37
10. R.D. Waldron, Phys. Rev. 99 (1955) 1727.
11. S.A. Patil, S.M. Otari, V.C. Mahajan, A.B. Patil et al. Solid State Commun. 78(1) (1991) 39.
12. S.A. Mazen, M.H. Abdallah, B.A. Sabrah, H.A.M. Hashem, Phys. Stat. Sol. (a) 134 (1992) 263-271.
13. A.M. El-Sayed, Ceram. Inter. 28 (2002) 651-655.
14. E.C. Stoner and E.P. Wohlfarth, Phil. Trans. Roy. Soc. A 240 (1948) 599; Reprinted by IEEE Trans. Magn. 27 (1991) 3475.
15. S. H. Liou, S. Huang, E. Klimek, and R. D. Kirby, J. Appl. Phys. 85, 4334 (1999)
16. P.K. Roy, J. Bera, J. Magn. Magn. Mater. 320 (2008) 1128.
17. Sagar E. Shirsath, R. H. Kadam, Anil S. Gaikwad, Ali Ghasemi, Akimitsu Morisako, J. Magn. Magn. Mater. 323 (2011) 3104-3108